JASA ARTICLE

Experimental study of airfoil-rotor interaction noise by wavelet beamforming

Wangqiao Chen,[1,a)] Bo Peng,[2] Rhea P. Liem,[2] and Xun Huang[1,b)]
[1]*Peking University, 100871 Beijing, China*
[2]*Hong Kong University of Science and Technology, Clear Water Bay, Kowloon, Hong Kong*

ABSTRACT:
A wavelet-based beamforming method is performed in this investigation to analyze moving acoustic sources in the time-frequency domain, which is of scientific significance and practical importance. The particular problem considered here is the interaction noise from an airfoil and the downstream rotor in the presence of a moving flow, which could find realistic applications in next-generation underwater and aviation systems. A realistic experimental setup is prepared with a rotating blade and the airfoil in an anechoic wind tunnel. The results show that the wavelet-based beamforming method is very suitable for unsteady sound source imaging, which would be able to strengthen the time-frequency analysis capability of acoustic imaging tests and, consequently, possibly leads to deepened physical insights of various transient and moving systems in underwater and aerospace systems.
 https://doi.org/10.1121/10.0001209

(Received 21 November 2019; revised 8 April 2020; accepted 19 April 2020; published online 6 May 2020)
[Editor: Michael J. White] Pages: 3248–3259

I. INTRODUCTION

In this paper, we aim to study flow-induced noise from the aerodynamic interaction between an airfoil and rotating blades. Applications can be found in unmanned aerial vehicle (UAV) and heating, ventilation, and air conditioning systems. To help the design of such a system of low noise, passive acoustic imaging with beamforming[1,2] is typically used to gain physical insights. Beamforming approaches[2–6] have been commonly employed for acoustic imaging for electrically and mechanically driven rotating machines.[7–9] The classical beamforming method of delay-and-sum type[10–12] has remained popular in industrial applications, mainly for its robust performance[13] in terms of the rejection of background noise and interference.[14] Recently, revolutionary approaches such as the deconvolution approach for the mapping of acoustic sources,[15] CLEAN based on spatial source coherence,[16] orthogonal,[17] adaptive,[18] and compressive sensing based methods[19] have been proposed to improve the associated spatial imaging resolution. In the works mentioned above, the noise source is assumed stationary, which enables statistical manipulations to improve the imaging quality. However, the imaging performance would be compromised for moving sources, which imposes a difficult trade-off between time-domain performance and frequency-domain performance.

In the case of stator-rotor interaction, in addition to the mechanical vibration noise, significant noise features also arise from the interaction between the airflow from stators (usually of an airfoil profile) and rotating fans. To capture such a rotating aerodynamic noise source, the classical beamforming method in the frequency domain has to adopt a short-time window for Fourier transform at the cost of decreased signal-to-noise ratio. Other available solutions include the rotating source identifier,[11,12] virtual rotating array,[20] and modal decomposition methods.[10,21] Figure 1 summarizes the categories of some of the most recent acoustic beamforming methods for rotating sources. Those methods have been tailored for some specific applications such as axial blade, helicopter, and wind turbine applications,[22–24] some of them, as the virtual rotating array method, require different operations and hardware setups from the classical beamforming approach.

In contrast, the recently proposed wavelet-based beamforming method[25] essentially follows the whole setup (and sensor array hardware) of the conventional beamforming approach and, theoretically, build up the time-frequency capability by replacing the inherent Fourier transform with wavelet transform. Wavelet is a powerful mathematical tool for time-frequency analysis,[26,27] which enables the development of beamforming methods from a totally new perspective.[28,29] Recent developments have shown its potentials in geological detection[30] and brain research.[31] For the completeness of the current paper, we would first introduce the essential concepts of the wavelet-based beamforming method. Then attention would be focused on the use of this method on a realistic aeroacoustic problem in anechoic wind tunnel experiments.

Compared to our previous report,[25] we wish to emphasize that the current paper offers more theoretical discussions and explanations on top of the experimental demonstrations. In this paper, the experimental results of the interaction noise between airfoils and rotating blades in

[a)]ORCID: 0000-0002-6158-7023.
[b)]Also at Hong Kong University of Science and Technology, Clear Water Bay, Kowloon, Hong Kong. Electronic mail: huangxun@pku.edu.cn

https://doi.org/10.1121/10.0001209

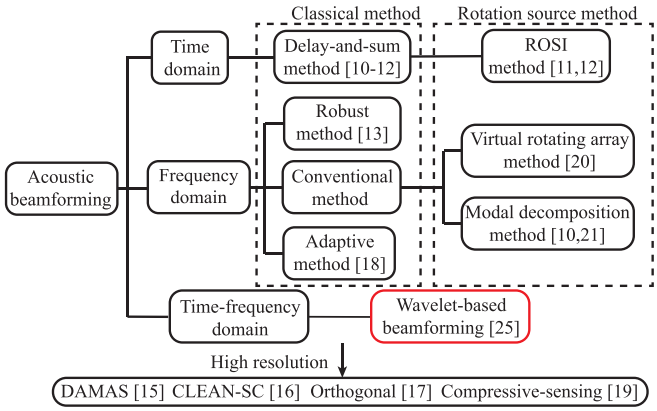

FIG. 1. (Color online) The historical development of acoustic beamforming methods.

anechoic wind tunnel are analyzed. In contrast, the former work has only considered a simplified problem setup without any flow interaction and only employed microphone array apparatus. To further demonstrate the effectiveness and potential of this new testing method, here we prepare experiments which combine particle image velocimetry (PIV) method and wavelet-based beamforming method together to reveal some interesting physical behaviors, which will constitute the main contributions of the current paper. The particular interest is focused on rotating fan and the corresponding stator-rotor interaction noise. We will show that the associated acoustic images could illustrate spatial-time-frequency features, thanks to the powerful capability of the wavelet transform.

The remaining part of this paper is organized as follows. First, the mathematically seemingly complicated

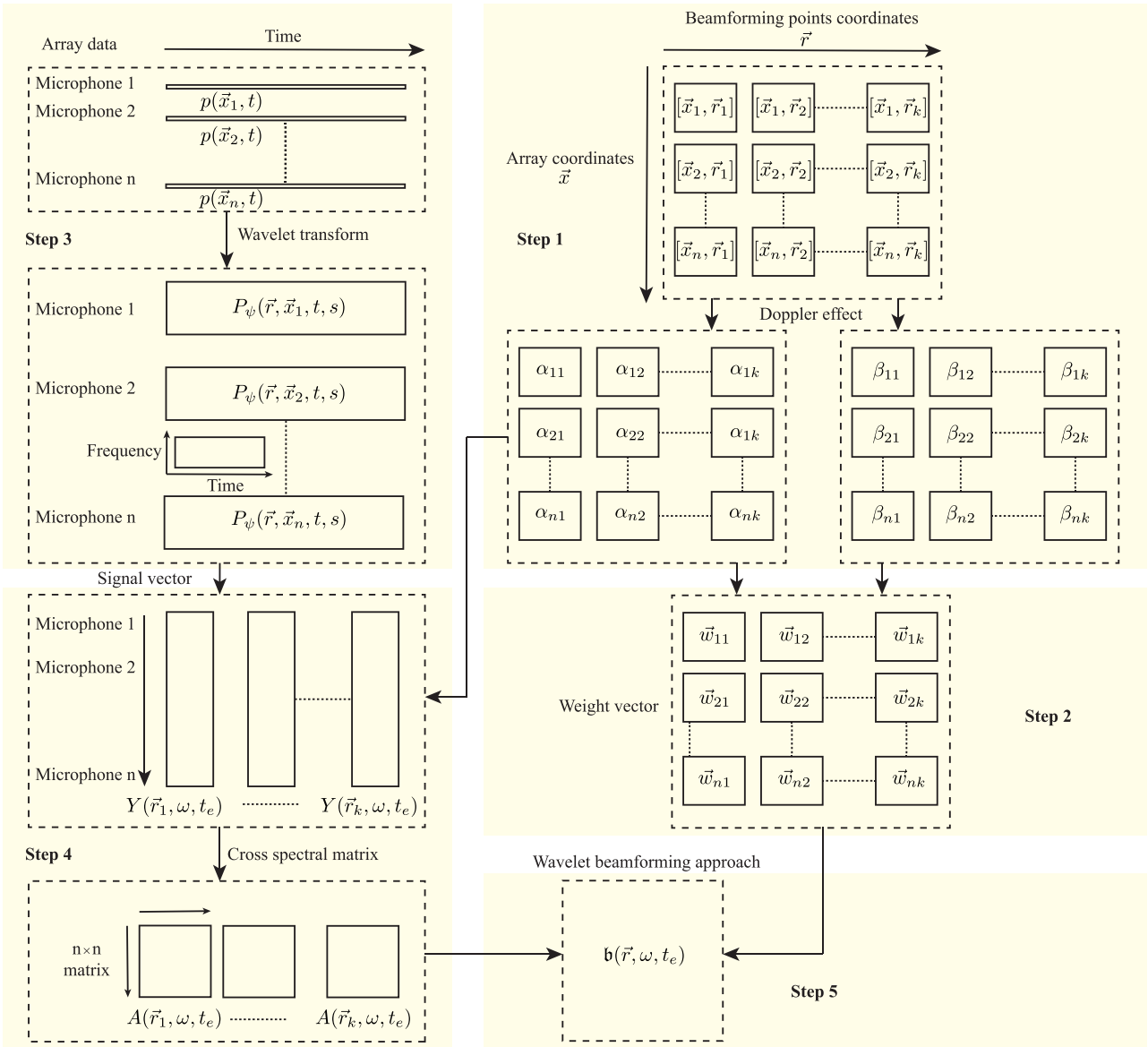

FIG. 2. (Color online) The algorithm steps of the proposed wavelet-based beamforming method. The left side follows steps (3) and (4), while the right side follows steps (1) and (2) and step (5).

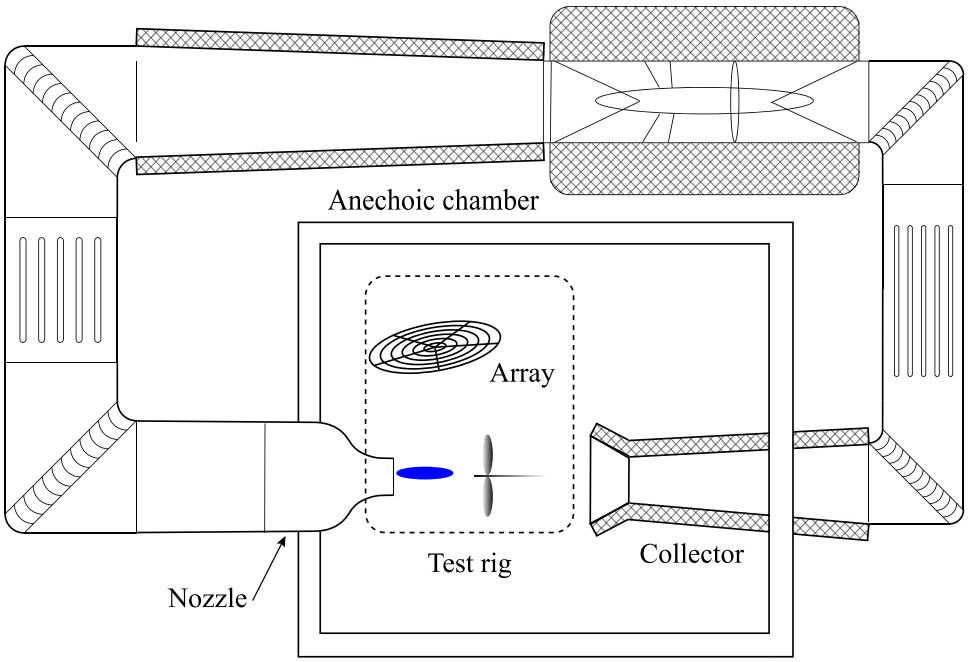

FIG. 3. (Color online) The plane view of the test rig with the wind tunnel.

procedure is summarized in Sec. II and show the wavelet-based beamforming method. Next, an experimental demonstration is discussed in Sec. III, which clearly shows the strength of the proposed new method from both physical and realistic perspectives. Finally, we present the concluding remarks in Sec. IV. Moreover, the analytical development and mathematical details can be found in the Appendixes.

II. THE TESTING METHOD

To provide a practical guideline for the implementation of the proposed method, we summarize the associated algorithm as shown in Fig. 2 for a sensor array system with n sensors and k acoustic imaging gridpoints. The subscript $(\cdot)_{i,j}$ denotes the variable that corresponds to the ith sensor and the jth imaging gridpoint. The algorithm implementation procedure is listed as the following steps.

(1) Calculate the parameters related to the Doppler effect, α and β, by following Eq. (A3) and Eq. (A4).
(2) Calculate the associated beamforming weight by Eq. (A18) for each sensor and imaging gridpoint.
(3) Set up the wavelet results by following Eq. (A5) (the map's signals from time domain into time-frequency domain).
(4) Construct the array measurement vector by Eq. (A15) and calculate the corresponding cross spectral matrix by Eq. (A16) (the cross spectral matrix is different at different time, frequency and beamforming location).
(5) Perform the wavelet-based beamforming for each imaging gridpoint consecutively by calculating Eq. (A19) and produce the final acoustic images.

In the above steps, all equations can be found in Appendix A.

III. EXPERIMENTAL DEMONSTRATION

In this paper, we focus on applying the proposed method in certain fan noise experiments of practical importance to demonstrate its capability in realistic setups. The experiments are carried out in an anechoic open-circuit wind tunnel with very low background noise (<36 dBA at the freestream speed $U_\infty = 10$ m/s). Figure 3 shows the plan view of the test rig inside the low-speed anechoic wind tunnel at the Hong Kong University of Science and Technology.

Figure 4 shows the schematics of the side view and plan view of the experimental setup, respectively, where a classical two blade propeller (DJI 9450 with the diameter $D = 240$ mm) is placed downstream to an airfoil (NACA 0020 with the chord length 100 mm), in the presence of the background mean flow from the nozzle of the wind tunnel. The Z-axis is from the center of the propeller and points

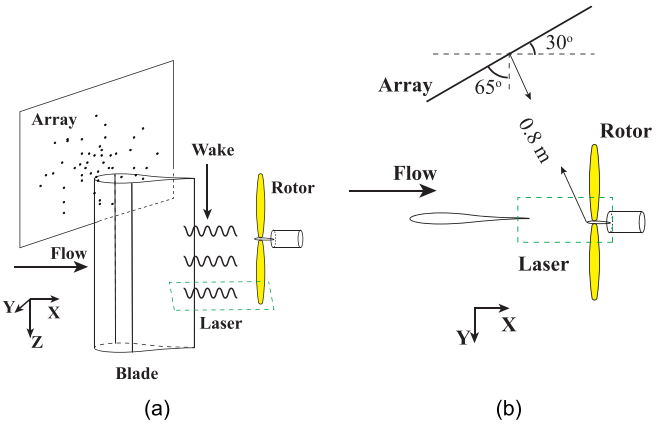

FIG. 4. (Color online) Schematics of the experimental setup, where (a) the side view and (b) the plan view. Here the rotating direction is clockwise and the instantaneous rotating axis points to the left.

https://doi.org/10.1121/10.0001209

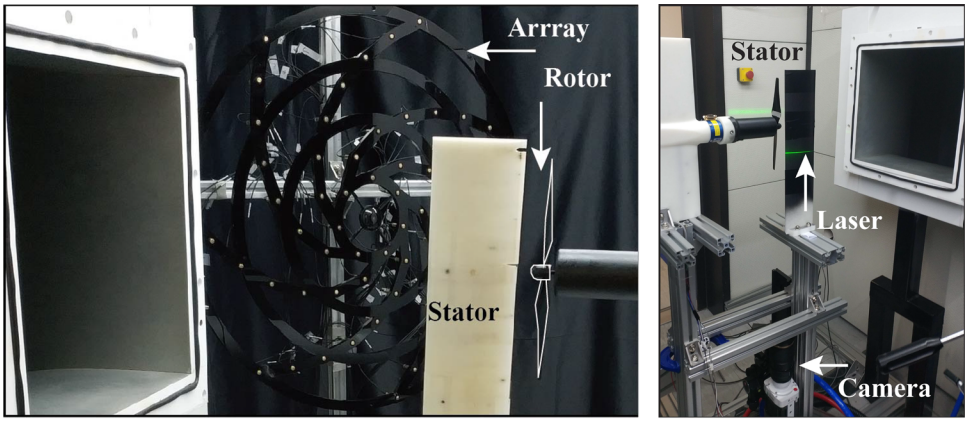

(a) (b)

FIG. 5. (Color online) The enlarged test section with the experimental setup that shows the microphone array and wind tunnel nozzle.

downward (as shown in Fig. 4). The Z-axis coordinate of the laser is at 0.375 D. The rotating axis is aligned with the X-axis, while the direction of angular velocity extends along the negative direction of the X-axis. The distance between the trailing edge of the airfoil and the leading-edge of the propeller is 0.105 D to observe the possible interaction. The chord-based Reynolds number at $U_\infty = 5\,\mathrm{m/s}$ is almost 5×10^4, which is already beyond the critical transition number of the NACA 0020 airfoil and the wake of the airfoil should already become turbulent. Figure 5 shows the microphone array, along with the model setups downstream to the nozzle of the anechoic wind tunnel.

To better explain the setups, Fig. 6(a) shows the definition of the phase angle. In this system, the phase varies from 0° to 360° in one rotating period, which corresponds to 0° to 180° angular locations for the two-blade rotor. The change of the phase angle within 180° includes the entire period of wake interaction with the blade. The definition of phase angle zero point is shown in the Fig. 6(a). Figures 6(b) and 6(c) show the coordinates associated with phase-averaged operations used in the analysis.

To provide physical insights, we first use PIV to visualize the flow field by injecting seeding (with a mean diameter of 2 μm), which is shown in Fig. 7(a). The particle density is six particles distributed in a 16×16 pixel window. These particles are first illuminated by a 1 mm thick double pulsed ND:YLF laser sheet and then captured by a SpeedLab 310 camera. The laser trigger signal and sound signal are recorded by the same acquisition card. The rotating state of the propeller is actively controlled by the proportional-integral-derivative method using an encoder and the controller from National Instruments. The visualization region and the field of view are represented by the dashed rectangle in Fig. 4. The raw images are processed by 2D adaptive correlation from the DynamicStudio software; an example of the resultant vorticity image is shown in Fig. 7(b), where the fixed airfoil (also called stator in the rest of this paper) and the rotor profile are represented by the solid lines. The dashed line denotes the analysis line which goes over the trailing edge of the wing and is parallel to the steamwise X axis. The "+" symbol marks the particular analysis point at the intersection between the analysis line and the cross-sectional area of the blades.

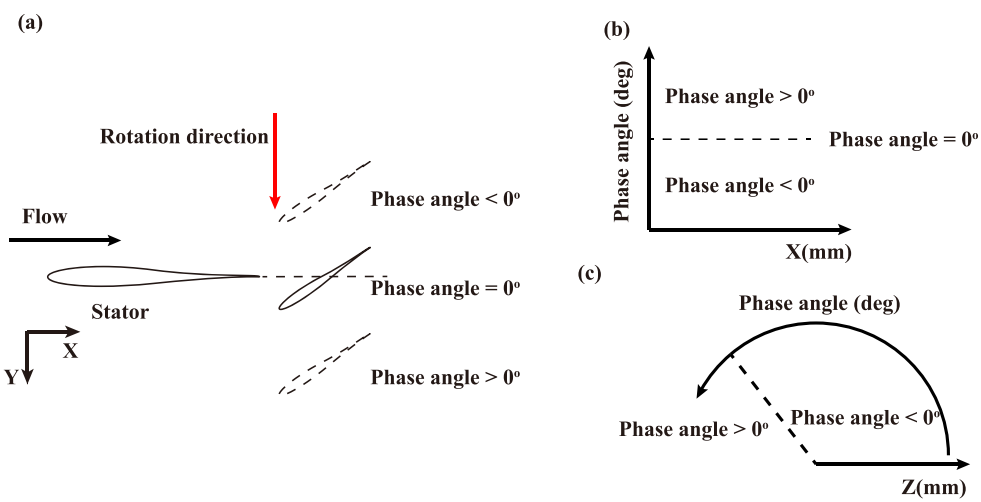

FIG. 6. (Color online) (a) The definition of the phase angle and (b), (c) the phase-averaged coordinates.

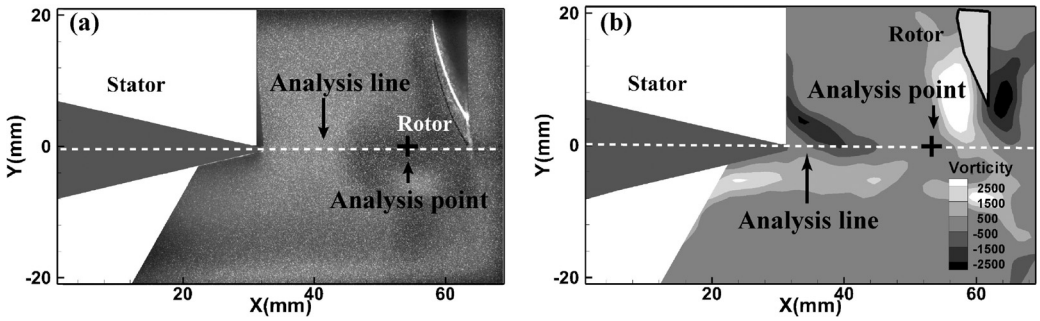

FIG. 7. The representative instantaneous vorticity contours obtained from the PIV measurements at $U_\infty = 5$ m/s and 4500 rpm, where (a) shows the image of particles and (b) the vorticity contours. The while contour shown in (a) at the top right is one of the rotating blades illuminated by laser sheets.

Figure 7 shows the plan view of some instantaneous PIV results with wind speed 5 m/s and propeller rotating speed 4500 rpm. It can be seen that the turbulent vorticity flow structures shedding from the trailing edge of the stator would impinge on the rotating propeller. Hence, the current experimental setup can be used to study the interaction between the turbulent flow structures and the rotating rotors. Such an interaction tends to produce strong flow-induced noise. The spectrum of the noise covers a broad range of frequencies, while the microphone array performs measurements at a much higher sampling frequency to show the corresponding physics of the flow-induced noise.

We investigate the airfoil-rotor interaction noise signature by using the proposed wavelet-based beamforming. We deploy a microphone array of 56 Brüel & Kjær type 4957 high-precision sensors (with a flat response between 50 Hz and 10 kHz). The layout of the microphones is multi-spiral and the detailed definition can be found in the Refs. 1, 18, while the diameter of the array is set to 0.7 m. In addition, the array is deliberately not aligned with the main flow to reduce any potential flow interference from the shear flow developing from the nozzle right outside the left corner of Fig. 4, at the expense of a compromised performance of the associated point spread function. All microphones are sampled simultaneously at 48 kHz for a total sampling period of 8.5 s. Furthermore, to enable a direct comparison with the PIV results, the trigger for the 1 kHz PIV laser and the acquisition of the 48 kHz acoustic sensing must be synchronous, that is, one laser illumination in every 48 sound wave measurements. Figure 8 shows the sound pressure level (SPL) results from a single microphone in the anechoic wind tunnel. The broadband noise at the high frequencies is mainly from trailing edge noise[33,34] and the half-blade passing frequency could be caused by the unsteady blade-rotor interaction.[35]

Figure 9 shows the phase locked results from the PIV measurements and the corresponding beamforming results at 4500 rpm. The first column shows the particle images at four different rotating phase angles. The second column shows the corresponding instantaneous phase-averaged vorticity contours obtained from the PIV measurements. The third column shows the corresponding phase-averaged beamforming results, where the dashed line and the solid line denote the X-location of the edges of the stator and rotor blades, respectively. PIV results shown in Fig. 9 can help to explain the fluid mechanisms of the wake-propeller interaction noise, while the wavelet beamforming results can illustrate the corresponding noise in time-frequency domain. Nevertheless, the PIV results suffer by low temporal resolution while the wavelet beamforming results are of low spatial resolution. Hence, the combination of the two complementary methods would be very helpful in aeroacoustic studies.

The first row in Fig. 9 (i.e., phase 1 at $-9°$) denotes the phase when the leading edge of the rotor interacts with the wake from the airfoil. The second row (phase 2 at 0°) corresponds to the phase when the wake impinges on the surface of one rotating blade. The third row (phase 3 at 9°) corresponds to the phase angle when the trailing edge of the rotor is about to leave the wake and the last row (phase 4 at 18°) corresponds to the phase angle when the rotor completely leaves the wake. The wavelet beamforming results in Fig. 9 clearly show the different sound source distributions of low- and high-frequencies with respect to different phases. In particular, when the blade cuts though the wake, the interaction noise at low frequencies becomes weaker, the noise at high frequencies increases, and the low-frequency source location moves away from the rotor. The above findings suggest that the generation mechanisms of the low-frequency part and the high-frequency part are different.

Figure 10 shows the beamforming results of low-frequency and Fig. 11 shows the beamforming results of

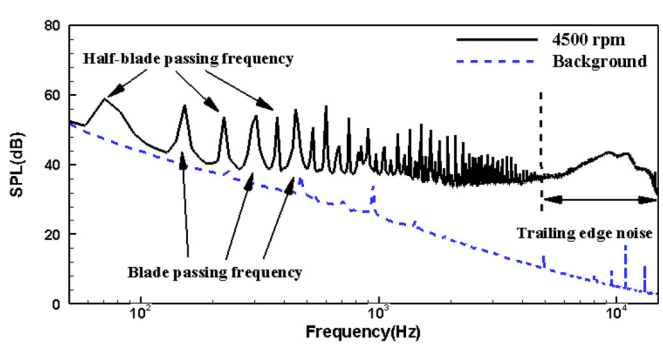

FIG. 8. (Color online) The SPL results for different experiment setups, where (—) is measured with 4500 rpm and (– –) is the facility background noise at 5 m/s.

https://doi.org/10.1121/10.0001209

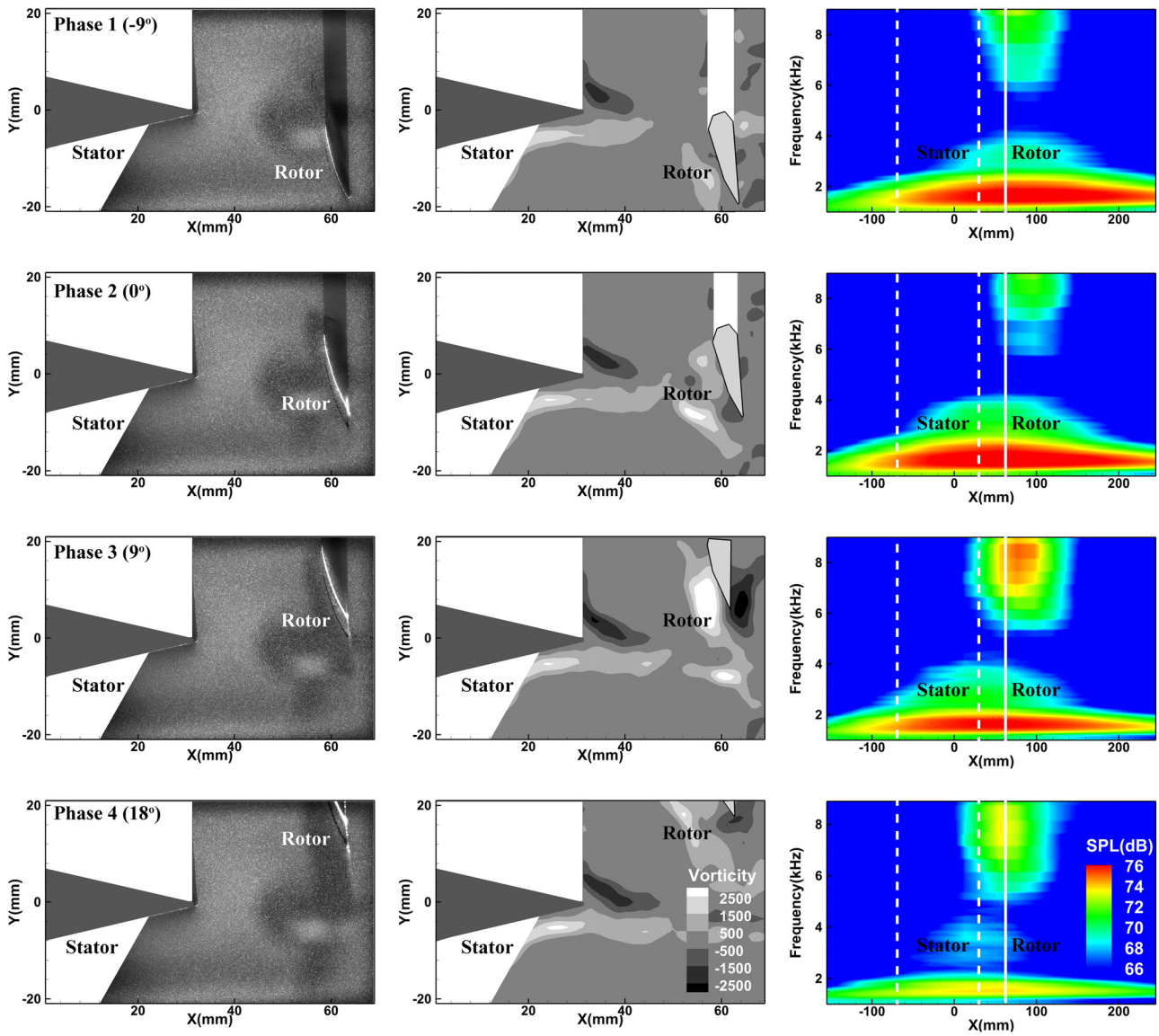

FIG. 9. (Color online) The phase locked PIV results and the wavelet-based beamforming results at 4500 rpm.

high-frequency (the corresponding coordinates are defined in Fig. 6). The white dashed lines are the location of the trailing edge of the stator and the leading edge of the rotor. The black dashed lines denote phase 1, 2, 3, and 4 that are the same as those shown in Fig. 9. In Fig. 10, along with the increase of frequency, the sidelobe of beamforming results gradually shrinks, but the source positions remain almost the same. At 4 kHz, the sound source distribution becomes distinctive on phase 3 and phase 4, which suggests that the trailing edge noise appear to be the dominant noise. In Fig. 11, the primary source always appears at phase 3 and phase 4. As shown in Fig. 9, phase 3 corresponds to the phase angle when the trailing edge of the rotor is about to leave the wake and the phase 4 corresponds to the phase angle when the rotor completely leaves the wake. The sound generated at phase 3 is from the interactions between the wake of stator and the rotor. The sound generated at phase 4 is mainly composed of flow interactions between the wake of stator and the disturbance from rotor. In Fig. 12, the vorticity intensity does not go down immediately. It shows that the disturbance of the blade to the wake area slowly disappears when the blade leaves the wake of the airfoil.

Moreover, the noise intensity changes as the rotating blades pass through the wake region. The rotating process of the blade will inevitably lead to the periodic disturbance of the wake. Figure 12 shows the phase-averaged vorticity intensity in the wake region, which is calculated alone the Y-axis at the position of 3 mm in front of the leading edge of the rotor. The phase angle is defined in Fig. 6. The symbols of selected phases shown as ■ in Fig. 12 are already defined in Fig. 9, and the symbol Δ denotes the maximum location of phase-averaged beamforming results, in Figs. 10 and 11, from 1.5 to 8 kHz. Physically, the beamforming results can be divided into two parts. The relatively low-frequency aeroacoustic sources from 1.5 to 4 kHz are mainly produced at phase 2 (0°). The other part from 4.5 to 8 kHz is mainly produced at phase

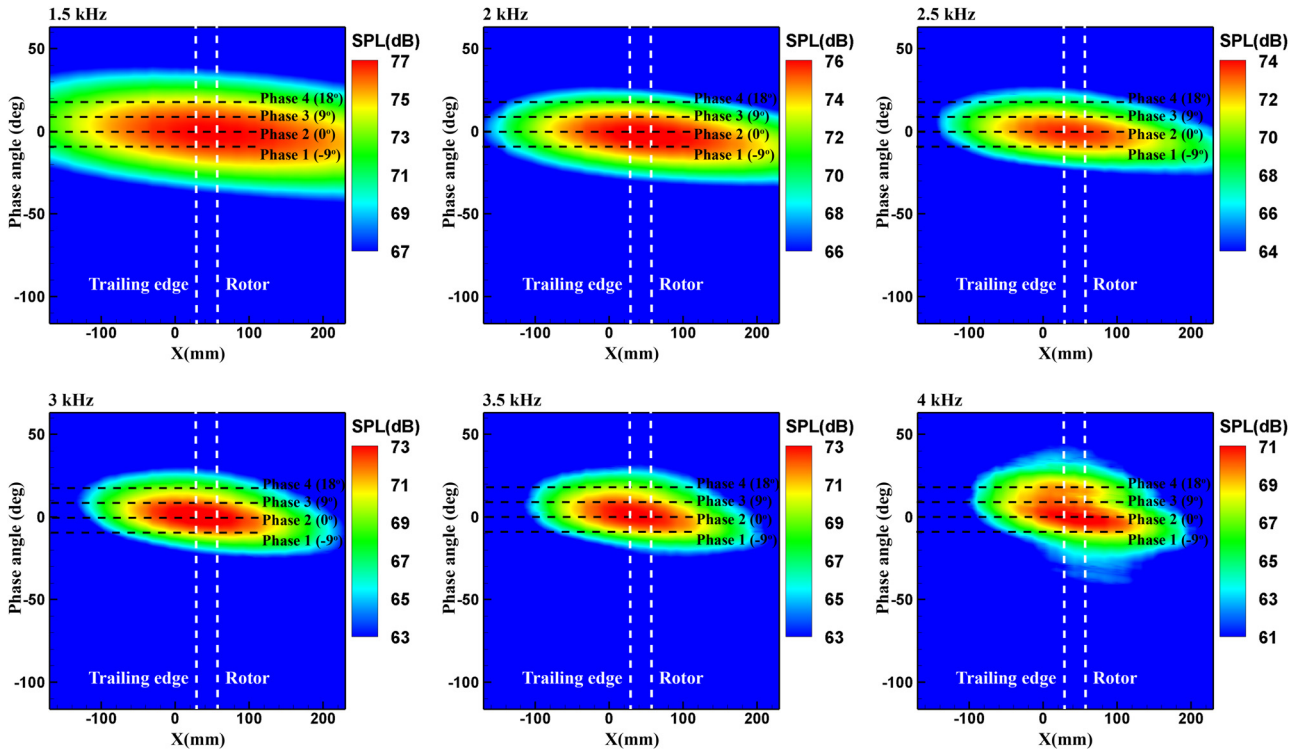

FIG. 10. (Color online) The relatively low-frequency beamforming results in phase-averaged coordinates with rotating speed 4500 rpm and wind speed 5 m/s.

3 (9°). As we shown in Fig. 9, phase 2 and phase 3 correspond to the phase angle when the wake impinges on the surface of one rotating blade and the phase angle when the trailing edge of the rotor is about to leave the wake. Hence, the relatively low-frequency noise is generated when the wake impinges on the rotating blade and should be loading noise in nature. On the other hand, the high-frequency noise is generated when the trailing edge of the rotor leaves the wake, where the turbulent flow downstream to the rotating blade should constitute the main noise source (see Fig. 8).

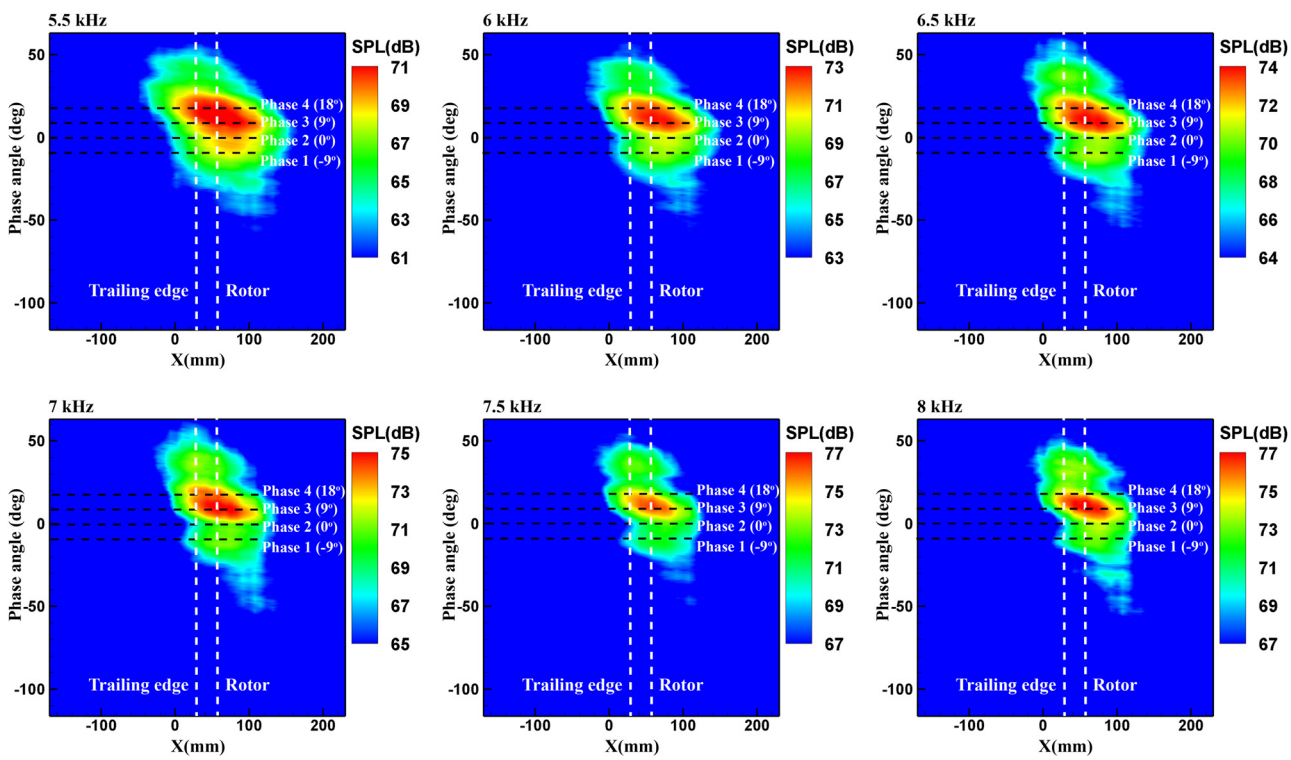

FIG. 11. (Color online) The high-frequency beamforming results in phase-averaged coordinates with rotating speed 4500 rpm and wind speed 5 m/s.

https://doi.org/10.1121/10.0001209

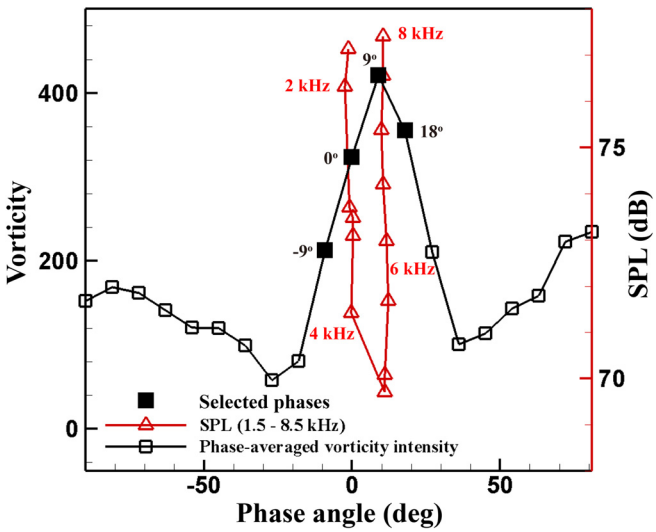

FIG. 12. (Color online) Phase-averaged vorticity intensity and SPL at 4500 rpm with wind speed 5 m/s.

Following the phase-averaged coordinates in Figs. 6(c), 13 and 14 show the phase-averaged beamforming results. Figure 13 shows the beamforming results in low-frequency and Fig. 14 shows the beamforming results in high-frequency. Similar to Figs. 10 and 11, low-frequency source mainly located at phase 1 and phase 2, high-frequency source mainly located at phase 3 and phase 4. The sound source distribution from phase 1 to phase 4 shows the noise in low-frequency mainly being generated when the leading edge of rotor cuts in the wake and ending when the trailing edge cuts out of the wake region.

In contrast to Fig. 11, the results shown in Fig. 14 contains the source distribution in the radials direction. The source of high-frequency is mainly located on the tip of the rotor. Again, it can be seen that the high-frequency noise is generated when the leading edge of the blade and the wake begin to interact with each other, which reaches its maximum value when the trailing edge of the blade is about to leave the wake area, and eventually disappears when the rotating blade is out of the airfoil wakes. Then, as discussed above, the main components of high-frequency noise are generated by turbulence in the third and fourth phase angles.

In summary, the airfoil-rotor interaction noise can be examined and analyzed by the proposed wavelet-based beamforming method. The whole physics processing of the airfoil-rotor interaction can be boiled down to four processes. First, the leading edge of the blade is gradually approaching the wake area, which produces weak noise at

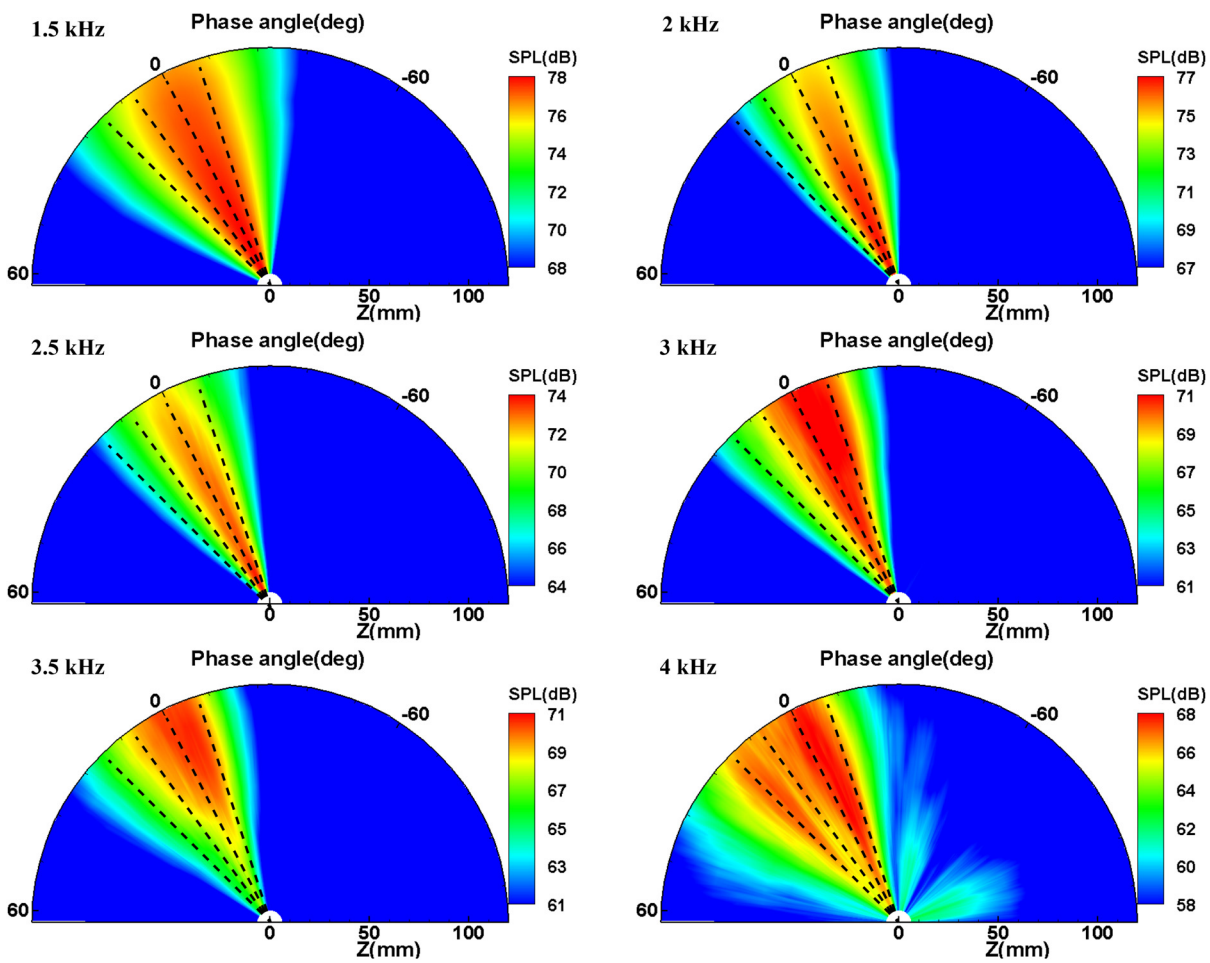

FIG. 13. (Color online) The low-frequency beamforming results in phase-averaged coordinates with rotating speed 4500 rpm and wind speed 5 m/s.

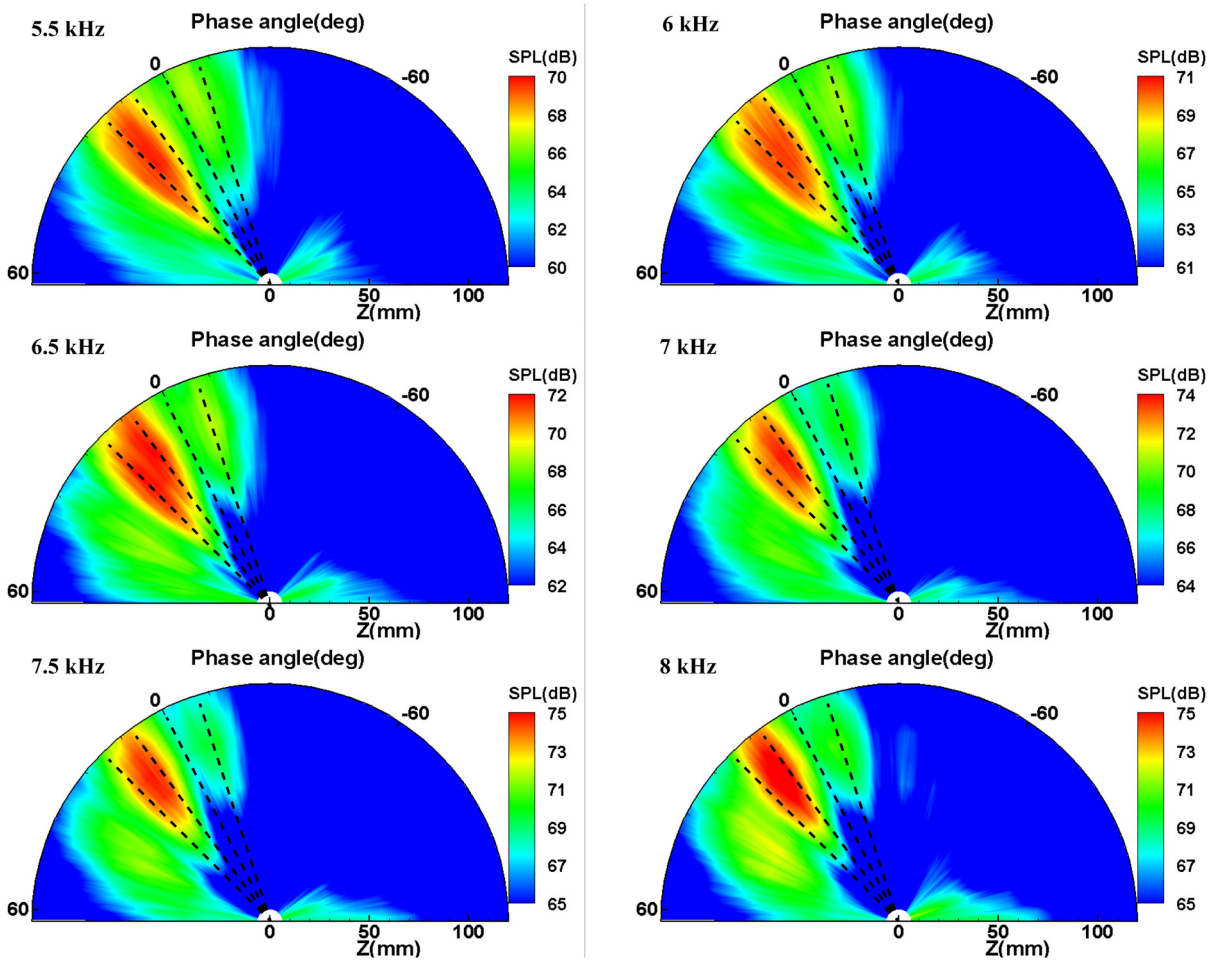

FIG. 14. (Color online) The relatively high-frequency beamforming results in phase-averaged coordinates with rotating speed 4500 rpm and wind speed 5 m/s.

all frequencies. Second, when the leading edge of the blade has interacted with the wake region, the loading noise of low-frequency starts to appear. Third, when the trailing edge of the rotor leaves the wake region, the trailing edge noise comes to be the dominated noise. Finally, after the blade leaves the wake region, the aerodynamic noise at all frequencies gradually diminishes.

IV. CONCLUSION

In this paper, a new time-frequency beamforming method has been proposed by utilizing the inherent powerful time-frequency analysis capability of the wavelet. It is conceivable that such a method would be especially useful for analyzing moving sources. The corresponding Green's function and the wavelet-based beamforming method have been developed in a pedagogical way, and the developed algorithm has been accompanied by a practical guideline to facilitate direct implementations for interested readers. Overall, the wavelet-based beamforming method is easy to implement and will be useful in time-frequency acoustic imaging applications.

Moreover, we have experimentally demonstrated the proposed new method in a particular stator-rotor setup, which could represent various turbomachineries[32] and motor driven systems. These demonstrations further highlighted the practical importance of our proposed method. It can be seen that the proposed wavelet-based method was able to successfully capture the equivalent flow-induced noise with improved imaging qualities. By this method, we analyzed the airfoil-rotor interaction noise and found that the generation of various types of noise is closely related to the relative motion of the rotating blades and the airfoil wakes. The combination of PIV and wavelet-based beamforming helps us identify the mechanism of noise generation. Consequently, the proposed new method would contribute to the development of sensing technology and physical studies.

ACKNOWLEDGMENTS

This work was partly supported by National Science Foundation of China (Grants Nos. 11772005 and 91852201), Ministry of Industry and Information Technology of China (Grant No. MJ-2015-F-012-03) and the Research Grants Council of the Hong Kong Special Administrative Region (Grant No. 16205317) and High-performance Computing Platform of Peking University.

https://doi.org/10.1121/10.0001209

APPENDIX A: WAVELET-BASED BEAMFORMING

This appendix provides a detailed derivation of the wavelet-based beamforming by employing a Green's function to model the moving source. Reference 25 gives a preliminary discussion of the associated mathematical background, which is extensively extended in this work by further taking account of the Doppler effect and the point-spread-function. For the completeness of the current paper, we introduce the whole process from scratch, which should guide readers of interest.

1. Green's function for the moving source

We first consider a point source with frequency ω and amplitude q_0, i.e., $q(t) = q_0 \exp(i\omega t)$, moving in a stationary medium with the instantaneous coordinates of $\vec{r}(t)$. The associated sound wave propagation is governed by the classical wave equation

$$\left(\frac{1}{c_0^2}\frac{\partial^2}{\partial t^2} - \nabla^2\right)\varphi(\vec{x},t) = q(t)\delta(\vec{r}(t) - \vec{x}), \tag{A1}$$

where c_0 is the speed of sound, φ is the acoustic potential, δ is the Dirac delta function, and $\vec{x}$ denotes the spatial coordinates. The free-space Green's function for the moving sound source can be written as[25]

$$G_w(\vec{r},\vec{x},t_e) = \frac{\alpha^2 \cdot \beta}{4\pi|\vec{x} - \vec{r}(t_e)|}. \tag{A2}$$

By using the Green's function, we can obtain the solution of Eq. (A1) as follows:

$$p(\vec{x},t) = \frac{\alpha^2\beta \cdot q'(t_e)}{4\pi|\vec{x} - \vec{r}(t_e)|}, \tag{A3}$$

where $(\cdot)'$ represents d/dt_e, and β collectively represents the acceleration effect of the moving source and the near-field effect. The symbol α represents the Doppler effect due to the moving of the source and t_e is the emission time of the source,

$$t_e = t - \left|\frac{\vec{x} - \vec{r}(t_e)}{c_0}\right|, \quad \frac{\partial t_e}{\partial t} = \alpha. \tag{A4}$$

2. The Doppler effect

In this article, we apply the $L1$-norm continuous wavelet transform to sound pressure p as follows:

$$P_\psi(\vec{r},\vec{x},t,s) = \frac{1}{s}\int_{-\infty}^{\infty} \psi^*\left(\frac{\tau - t}{s}\right) \cdot p(\vec{x},\tau)d\tau, \tag{A5}$$

where $(\cdot)^*$ denotes a complex conjugate and s is the scale parameter of the Morse wavelet ψ. We wish to mention that P_ψ contains a couple of parameters to represent the moving source in the time-frequency domain. Then, by substituting Eq. (A3) and (A2) into Eq. (A5), we obtain

$$P_\psi(\vec{r},\vec{x},t,s) = \frac{1}{s}\int_{-\infty}^{\infty} \psi^*\left(\frac{\tau - t}{s}\right) \cdot G_w(\vec{r},\vec{x},\tau_e)q'(\tau_e)d\tau, \tag{A6}$$

where τ_e is

$$\tau_e \triangleq \tau - \left|\frac{\vec{x} - \vec{r}(\tau_e)}{c_0}\right|, \tag{A7}$$

which follows the definition in Eq. (A4). Similarly, we define $d\tau_e/d\tau = \alpha_\tau$, which leads to $d\tau = d\tau_e/\alpha_\tau$. Then, by using the intermediate value theorem, we can have the following approximations:

$$\tau = \int \frac{d\tau_e}{\alpha_\tau(\tau_e)} \approx \frac{\tau_e}{\alpha_\tau(\hat{\tau})}, \quad t = \int \frac{dt_e}{\alpha(t_e)} \approx \frac{t_e}{\alpha}, \tag{A8}$$

where $\hat{\tau}$ is the intermediate point of τ_e in the whole integral interval.

Physically, if the wavelet decays rapidly, we can approximate the relationship between τ and τ_e by

$$\tau = \frac{\tau_e}{\alpha_\tau(\hat{\tau})} = \frac{\tau_e}{\alpha_\tau(t)} + \epsilon = \frac{\tau_e}{\alpha} + \epsilon, \tag{A9}$$

where ϵ is the approximation error, which tends to be zero when τ approaches zero. Hence, by setting $\epsilon = 0$, the wavelet transform in Eq. (A6) can be approximated by

$$P_\psi(\vec{r},\vec{x},t,s) \approx \frac{1}{s}\int_{-\infty}^{\infty} \psi^*\left(\frac{\tau_e - t_e}{\alpha s}\right) G_w(\vec{r},\vec{x},\tau_e)q'(\tau_e)\frac{d\tau_e}{\alpha}. \tag{A10}$$

When the change of $G(\vec{x},\tau_e)$ is much slower than that of the moving source, Eq. (A10) can be reduced to

$$P_\psi(\vec{r},\vec{x},t,s) = G_w(\vec{r},\vec{x},t_e)\int_{-\infty}^{\infty} \psi^*\left(\frac{\tau_e - t_e}{\alpha s}\right) q'(\tau_e)\frac{d\tau_e}{\alpha s}. \tag{A11}$$

Finally, if we define a new wavelet transform for q' as

$$Q(t_e,s) = \frac{1}{s}\int_{-\infty}^{\infty} \psi^*\left(\frac{\tau_e - t_e}{s}\right) q'(\tau_e)d\tau_e, \tag{A12}$$

we can simplify Eq. (A11) to

$$P_\psi\left(\vec{r},\vec{x},t,\frac{s}{\alpha}\right) = G_w(\vec{r},\vec{x},t_e) \cdot Q(t_e,s). \tag{A13}$$

We wish to emphasize here that the above simplification becomes invalid when the moving frequency is greater than the frequency of the moving sound source.

Next, according to the relationship between the scale parameter and the frequency,[28] we have

$$\omega(s) = 2\pi \frac{f_0}{s} \cdot T_s, \tag{A14}$$

where f_0 is the peak frequency and T_s is the sampling time interval. Further, it is easy to understand that the frequency perceived by a receiver, ω_r, is different from the frequency of the source, ω, due to the Doppler effect. For the current setup, we represent this relationship as $\omega_r = \alpha \cdot \omega$.

3. Wavelet-based beamforming

Now, we start to construct the wavelet-based beamforming approach for the moving sound source. First, we define the notations for the receivers of a sensor array of n microphones. Here we use $\vec{x}_j$ to denote the coordinates of the j-th sensor, t_j the corresponding receiving time, and $\vec{r}$ the coordinates of the acoustic imaging gridpoint. Then, after applying the wavelet transform, Eq. (A13) shows that the array measurements would form the following vector:

$$Y(\vec{r}, \omega, t_e) = \left[P_\psi\left(\vec{r}, \vec{x}_1, t_1, \frac{s}{\alpha}\right), \ldots, P_\psi\left(\vec{r}, \vec{x}_n, t_n, \frac{s}{\alpha}\right) \right]. \tag{A15}$$

The associated array cross spectral matrix would be

$$A(\vec{r}, \omega, t_e) = Y(\vec{r}, \omega, t_e) \cdot Y^*(\vec{r}, \omega, t_e). \tag{A16}$$

We wish to emphasize here that Eq. (A15) and Eq. (A16) contain both frequency ω and the emission time t_e, which distinguish our method from the classical beamforming method.

We further define a vector

$$\vec{G}_w(\vec{r}, t_e) = [G_w(\vec{r}, \vec{x}_1, t_e), \ldots, G_w(\vec{r}, \vec{x}_n, t_e)], \tag{A17}$$

which enables us to simply define the wavelet-based beamforming weight vector as

$$\vec{w}_w(\vec{r}, t_e) = \frac{\vec{G}_w(\vec{r}, t_e)}{||\vec{G}_w(\vec{r}, t_e)||}, \tag{A18}$$

where $||\cdot||$ represents the $L2$-norm. Finally, by following the classical analytical form of conventional beamforming approaches,[18] we propose the new wavelet-based beamforming as

$$\mathfrak{b}_{wavelet}(\vec{r}, \omega, t_e) = \vec{w}_w^*(\vec{r}, t_e) A(\vec{r}, \omega, t_e) \vec{w}_w(\vec{r}, t_e). \tag{A19}$$

It is easy to see that the proposed wavelet-based beamforming method would reduce to conventional beamforming when the sound source becomes stationary in time space. One key feature of the wavelet-based beamforming discussed above is that this method enables us to analyze signals in time, spatial, and frequency domains simultaneously, which shall lead to profound physical insights of certain physical problems.

4. Point-spread-function

The point-spread-function (PSF) of wavelet-based beamforming depends on time and frequency domains. Following the PSF developed in conventional beamforming method,[1] the new PSF is defined as

$$\mathfrak{p}_w(\vec{r}_b, \vec{r}_s, t_e) = \left| \vec{w}^*(\vec{r}_b, t_e) \cdot \frac{Y(\vec{r}_b, \omega, t_e)}{||G(\vec{r}_s, t_e)||} \right|^2, \tag{A20}$$

where the subscripts $(\cdot)_s$ and $(\cdot)_b$ refer to the variables of the source point and beamforming point, respectively. We can then express the $L1$-norm continuous wavelet transform to sound pressure $\mathfrak{q}$ generated at $\vec{r}_s$ (with normalized amplitude) as

$$P_\psi(\vec{r}, \vec{x}, t, s) = G_w(\vec{r}_s, \vec{x}, t_e + \delta t) \times \int_{-\infty}^{\infty} \psi^*\left(\frac{\tau_e - t_e}{\alpha_s s}\right) \mathfrak{q}'(\tau_e + \delta t) \frac{d\tau_e}{\alpha_s s}, \tag{A21}$$

where δt is given as

$$\delta t = \frac{|\vec{r}_b - \vec{x}| - |\vec{r}_s - \vec{x}|}{c_0}. \tag{A22}$$

By neglecting the time variations of α and β, Eq. (A21) can be approximated by

$$P_\psi\left(\vec{r}, \vec{x}, t, \frac{s}{\alpha_b}\right) = G_w(\vec{r}_s, \vec{x}, t_e) Q(t_e + \delta t, s), \tag{A23}$$

where Q is

$$Q(t_e + \delta t, s) = \int_{-\infty}^{\infty} \psi^*\left(\frac{\tau_e - t_e}{s} \frac{\alpha_b}{\alpha_s}\right) \mathfrak{q}'(\tau_e + \delta t) \frac{\alpha_b}{\alpha_s} \frac{d\tau_e}{s}. \tag{A24}$$

From Eq. (A24), we define a diagonal matrix $\tilde{Q}$, where each element is

$$\tilde{Q}_{ij} = \int_{-\infty}^{\infty} \psi^*\left(\frac{\tau_e - t_e}{s} \frac{\alpha_b(\vec{x}_j)}{\alpha_s(\vec{x}_j)}\right) \mathfrak{q}'(\tau_e + \delta t) \frac{\alpha_b(\vec{x}_j)}{\alpha_s(\vec{x}_j)} \frac{d\tau_e}{s} \cdot \delta_{ij} \tag{A25}$$

and $\delta_{ij} = 1$ when $i = j$ and otherwise $\delta_{ij} = 0$. We can then use $\tilde{Q}$ to simplify Eq. (A20) to

$$\mathfrak{p}_w(\vec{r}_b, \vec{r}_s, t_e) = |\vec{w}^*(\vec{r}_b, t_e) \cdot (\vec{w}(\vec{r}_s, t_e) \cdot \tilde{Q})|^2. \tag{A26}$$

When the source is stable, $\mathfrak{p}_w$ would reduce to the classical PSF in conventional beamforming.

APPENDIX B: THE INTERPRETATION OF THE ALGORITHM STEPS

Considering the acoustic imaging for moving source, the biggest challenge is the shifted frequency influenced by

the Doppler effect. Thus, we need do time-delay to capture the same wave front as that in the delay-and-sum method, and then choose accurate frequency to generate the CSM as that was defined in the conventional beamforming method.

Step 1 would calculate the parameters related to the Doppler effect. Step 2 would calculate the associated beamforming weight vector as conventional beamforming. Step 3 employs wavelet transform to map signal from time domain into time-frequency domain. Then we conduct the time delay as that in the delay-and-sum method and choose the vector from the different frequency, which have been shift by α and β from step 1. Then we would have the CSM of every considered location and time (which is performed in step 4). Finally, step 5 produces the wavelet-based beamforming results.

[1]T. J. Mueller, *Aeroacoustic Measurements* (Springer-Verlag, Berlin), Chap. 2, p. 77 (2002).
[2]R. Merino-Martínez, P. Sijtsma, M. Snellen, T. Ahlefeldt, J. Antoni, C. J. Bahr, D. Blacodon, D. Ernst, A. Finez, S. Funke, T. F. Geyer, S. Haxter, G. Herold, X. Huang, W. M. Humphreys, Q. Leclère, A. Malgoezar, U. Michel, T. Padois, A. Pereira, C. Picard, E. Sarradj, H. Siller, D. G. Simons, and C. Spehr, "A review of acoustic imaging methods using phased microphone arrays," CEAS Aeronaut. J. **10**(1), 197–230 (2019).
[3]B. D. Van Vee and K. M. Buckley, "Beamforming: A versatile approach to spatial filtering," IEEE ASSP Mag. **5**(2), 4–24 (1988).
[4]S. Bousabaa, J. Bulté, D. Mincu, R. Marchiano, and F. Ollivier, "Sparse Green's functions estimation using orthogonal matching pursuit: Application to aeroacoustic beamforming," AIAA J. **56**(6), 2252–2270 (2018).
[5]S. Abadi, K. Haworth, K. Mercado-Shekhar, and D. Dowling, "Frequency-sum beamforming for passive cavitation imaging," J. Acoust. Soc. Am. **144**(1), 198–209 (2018).
[6]X. Huang, "Real-time location of coherent sound sources by the observer-based array algorithm," Meas. Sci. Technol. **22**(6), 065501 (2011).
[7]W. J. Yu and X. Huang, "Compressive sensing based spinning mode detections by in-duct microphone arrays," Meas. Sci. Technol. **27**(5), 055901 (2016).
[8]M. Debrouwere and D. Angland, "Airy pattern approximation of a phased microphone array response to a rotating point source," J. Acoust. Soc. Am. **141**(2), 1009–1018 (2017).
[9]F. Krömer, J. Müller, and S. Becker, "Investigation of aeroacoustic properties of low-pressure axial fans with different blade stacking," AIAA J. **56**(4), 1507–1518 (2018).
[10]W. Pannert and C. Maier, "Rotating beamforming-motion-compensation in the frequency domain and application of high-resolution beamforming algorithms," J. Sound Vib. **333**(7), 1899–1922 (2014).
[11]P. Sijtsma, S. Oerlemans, and H. Holthusen, "Location of rotating sources by phased array measurements," in *7th AIAA/CEAS Aeroacoustic Conference*, AIAA paper 2001-2167 (2001).
[12]P. Sijtsma, "Using phased array beamforming to locate broadband noise sources inside a turbofan engine," National Aerospace Laboratory, Report No. NLR-TP-2009-689 (2006).
[13]H. Cox, R. Zeskind, and M. Owen, "Robust adaptive beamforming," IEEE Trans. Acoust. Speech Sign. Process. **35**(10), 1365–1376 (1987).
[14]R. A. Gramann and J. W. Mocio, "Aeroacoustic measurements in wind tunnels using adaptive beamforming methods," J. Acoust. Soc. Am. **97**(6), 3694–3701 (1995).
[15]T. Brooks and W. Humphreys, "A deconvolution approach for the mapping of acoustic sources (DAMAS) determined from phased microphone arrays," J. Sound Vib. **294**(4), 856–879 (2006).
[16]P. Sijtsma, "CLEAN based on spatial source coherence," Int. J. Aeroacoust. **6**(4), 357–374 (2007).
[17]E. Sarradj, "A fast signal subspace approach for the determination of absolute levels from phased microphone array measurements," J. Sound Vib. **329**(9), 1553–1569 (2010).
[18]X. Huang, L. Bai, I. Vinogradov, and E. Peers, "Adaptive beamforming for array signal processing in aeroacoustic measurements," J. Acoust. Soc. Am. **131**(3), 2152–2161 (2012).
[19]S. Zhong, Q. Wei, and X. Huang, "Compressive sensing beamforming based on covariance for acoustic imaging with noisy measurements," J. Acoust. Soc. Am. **134**(5), EL445–EL451 (2013).
[20]R. Dougherty and B. Walker, "Virtual rotating microphone imaging of broadband fan noise," in *15th AIAA/CEAS Aeroacoustic Conference/ 30th AIAA Aeroacoustic Conference*, AIAA paper 2009-3121 (2009).
[21]S. Guérin and C. Weckmüller, "Frequency-domain reconstruction of the point-spread function for moving sources," in *2nd Berlin Beamforming Conference* (2008).
[22]G. Herold and E. Sarradj, "Microphone array method for the characterization of rotating sound sources in axial fans," Noise Control Eng. J. **63**(6), 546–551 (2015).
[23]G. Herold, C. Ocker, E. Sarradj, and W. Pannert, "Comparison of microphone array methods for the characterization of rotating sound sources," in *7th Berlin Beamforming Conference* (2018).
[24]C. Ocker and W. Pannert, "Imaging of broadband noise from rotating sources in uniform axial flow," AIAA J. **55**(4), 1185–1193 (2016).
[25]W. Q. Chen and X. Huang, "Wavelet-based beamforming for high-speed rotating acoustic source," IEEE Access **6**, 10231–10239 (2018).
[26]M. Biswal and S. Mishra, "Comparison of time-frequency methods for analyzing stimulus frequency otoacoustic emissions," J. Acoust. Soc. Am. **143**(2), 626–639 (2018).
[27]R. Liu, S. Xu, H. Hu, R. Huo, S. Wang, and M. Wan, "Wavelet-transform-based active imaging of cavitation bubbles in tissues induced by high intensity focused ultrasound," J. Acoust. Soc. Am. **140**(2), 798–805 (2016).
[28]J. Lilly and S. Olhede, "Generalized morse wavelets as a superfamily of analytic wavelets," IEEE Trans. Sign. Process. **60**(11), 6036–6041 (2012).
[29]W. Xu, T. C. Liu, and H. Schmidt, "Beamforming based on spatial-wavelet decomposition," in *Sensor Array and Multichannel Signal Processing Workshop Proceedings* (2002), pp. 480–484.
[30]F. Wassermann, "Locating the sources of volcanic explosions and volcanic tremor at Stromboli volcano (Italy) using beam-forming on diffraction hyperboloids," Phys. Earth Planet. Int. **104**(1-3), 271–281 (1997).
[31]J. Xiang, Y. Liu, Y. Wang, R. Kotecha, E. G. Kirtman, Y. Chen, X. Huo, H. Fujiwara, N. Hemasilpin, T. deGrauw, and D. Rose, "Neuromagnetic correlates of developmental changes in endogenous high-frequency brain oscillations in children: A wavelet-based beamformer study," Brain Res. **1274**, 28–39 (2009).
[32]X. Zhang, "Aircraft noise and its nearfield propagation computations," Acta Mech. Sin. **28**(4), 960–977 (2015).
[33]H. Murray, W. Devenport, W. Alexander, S. Glegg, and D. Wisda, "Aeroacoustics of a rotor ingesting a planar boundary layer at high thrust," J. Fluid Mech. **850**, 212–245 (2018).
[34]H. Murray, "Turbulence and sound generated by a rotor operating near a wall," Master's thesis, Virginia Polytechnic Institute and State University, Blacksburg, VA (2016).
[35]R. Martin, J. Hardin, "Spectral characteristics of rotor blade/vortex interaction noise," J. Aircraft **25**(1), 62–68 (1988).